High-Precision Mapping of Diamond Crystal Strain Using Quantum Interferometry

Mason C. Marshall,[1,2,3,*,‡] Reza Ebadi,[3,4] Connor Hart,[3] Matthew J. Turner,[3] Mark J.H. Ku,[3,5,6] David F. Phillips,[2] and Ronald L. Walsworth[1,2,3,4,†]

[1] *Department of Electrical and Computer Engineering, University of Maryland, College Park, Maryland 20742, USA*

[2] *Center for Astrophysics, Harvard & Smithsonian, Cambridge, Massachusetts, 02138, USA*

[3] *Quantum Technology Center, University of Maryland, College Park, Maryland, 20742, USA*

[4] *Department of Physics, University of Maryland, College Park, Maryland 20742, USA*

[5] *Department of Physics and Astronomy, University of Delaware, Newark, Delaware 19716, USA*

[6] *Department of Materials Science and Engineering, University of Delaware, Newark, Delaware 19716, USA*

(Received 27 July 2021; revised 11 November 2021; accepted 3 December 2021; published 15 February 2022)

Crystal-strain variation imposes significant limitations on many quantum sensing and information applications for solid-state defect qubits in diamond. Thus, the precision measurement and control of diamond crystal strain is a key challenge. Here, we report diamond strain measurements with a unique set of capabilities, including micron-scale spatial resolution, a millimeter-scale field of view, and a 2-order-of-magnitude improvement in volume-normalized sensitivity over previous work, reaching $5(2) \times 10^{-8}/\sqrt{\text{Hz}\ \mu\text{m}^{-3}}$ (with spin-strain coupling coefficients representing the dominant systematic uncertainty). We use strain-sensitive spin-state interferometry on ensembles of nitrogen-vacancy (N-V) color centers in single-crystal bulk diamond with low strain gradients. This quantum interferometry technique provides insensitivity to magnetic-field inhomogeneity from the electronic and nuclear spin bath, thereby enabling long N-V–ensemble electronic spin dephasing times and enhanced strain sensitivity, as well as broadening the potential applications of the technique beyond isotopically enriched or high-purity diamond. We demonstrate the strain-sensitive measurement protocol first on a confocal scanning laser microscope, providing quantitative measurement of sensitivity as well as three-dimensional strain mapping; and second on a wide-field-imaging quantum diamond microscope. Our strain-microscopy technique enables fast, sensitive characterization for diamond material engineering and nanofabrication; as well as diamond-based sensing of strains applied externally, as in diamond anvil cells or embedded diamond stress sensors, or internally, as by crystal damage due to particle-induced nuclear recoils.

DOI: 10.1103/PhysRevApplied.17.024041

I. INTRODUCTION

Quantum defects in diamond are a leading platform for many applications, ranging from magnetometry and magnetic imaging [1–8] to quantum networking and communication [9,10]. Such applications leverage the long spin coherence times and straightforward optical control of diamond-defect qubits [11,12], as well as the capability to engineer diamond with a tunable defect density and geometry [7,13], and to integrate qubits into photonic nanostructures [14,15]. These applications also critically depend on the host environment; e.g., diamond crystal-strain inhomogeneity limits magnetometry by broadening and shifting qubit spin transitions [16], degrades the coherence of ensemble and single qubits [7,17,18], and spectrally broadens or quenches qubits near fabricated nanostructures [19]. The sensitive measurement of diamond strain is thus a key enabling technique for quantum applications and, as such, has been the subject of significant recent study [16,20,21].

Beyond this negative role, diamond strain can also have utility in quantum applications. Control of qubit couplings via the strain environment can enable quantum metrology or networking [18,22–24] or drive qubit transitions [25,26]. Strain-mediated couplings also underlie hybrid quantum-nanomechanical systems [27,28]. Small diamonds as *in situ* strain sensors can be widely, deployed, as in high-pressure anvil cells or in curing amorphous solids [29,30]. Finally, sensitive measurements

*mason.marshall@nist.gov

†walsworth@umd.edu

‡Current address: Time and Frequency Division, NIST, Boulder, Colorado 80305, USA.

of damage-induced strain in diamond are essential to proposed diamond-based particle detectors, such as for directional detection of dark matter consisting of weakly interacting massive particles (WIMPs) [31,32].

Improvements in sensitive diamond strain measurement are therefore of broad importance. Several techniques have been developed for the measurement of diamond crystal strain; however, quantum applications require fast sensing of small strains at relevant length scales, demanding state-of-the-art volume-normalized sensitivity. X-ray tomography and microscopy require long data-acquisition times (and, frequently, synchrotron beamline access) [33–35]; Raman spectroscopy faces a detection noise floor near a strain of 10^{-5}, far from the state of the art [36,37]; and birefringence imaging integrates light through an entire diamond, limiting spatial resolution [16,38].

Here, we report strain measurements with a volume-normalized sensitivity of $5(2) \times 10^{-8}/\sqrt{\text{Hz}\ \mu\text{m}^{-3}}$ (with spin-strain coupling coefficients representing the dominant systematic uncertainty)—an improvement by 2 orders of magnitude over previous work [16]. Using spin-state interferometry of an ensemble of nitrogen-vacancy (N-V) centers, we achieve high precision via a strain-sensitive measurement protocol designed to be insensitive to static and low-frequency magnetic fields. We apply this procedure to single-crystal chemical-vapor-deposition (CVD) bulk diamond material grown by Element Six Ltd., with 99.995% ^{12}C and an estimated N-V density of approximately 0.4 parts per million (ppm), featuring low strain and a long N-V ensemble spin dephasing time of $T_2^\star = 7.5\ \mu$s (for additional details, see Appendix B). We first study strain in this diamond using a confocal scanning laser microscope; the known confocal volume allows us to quantitatively characterize the volume-normalized strain sensitivity and to demonstrate three-dimensional mapping of strain features in the diamond with micron-scale resolution. We then apply the interferometry protocol using a wide-field quantum diamond microscope (QDM) [1,39,40], which provides high-sensitivity strain imaging of a millimeter-scale diamond section. These results provide a benchmark for sensitive mapping of diamond strain with a unique combination of spatial resolution, field of view, and sensitivity; they thereby open a path to applications such as characterization and engineering of diamonds for quantum information and metrology, *in situ* strain measurements using micron-scale diamonds in soft materials, and a future dark-matter search [31,32].

We note that while the strain sensitivity achieved here leverages a high density of N-V centers, this technique is generally applicable to diamonds with any N-V density. All else being equal, the sensitivity improves with the square root of the N-V density. Additionally, while these measurements use isotopically purified diamond, the insensitivity of the quantum interferometry technique to magnetic field inhomogeneity will enable precise strain measurements in diamonds with higher impurity or ^{13}C content—expanding the utility of strain sensing beyond specially engineered quantum diamonds.

II. N-V–CENTER SPECTROSCOPY OVERVIEW

Traditional techniques for the measurement of diamond strain are limited in volume-normalized sensitivity by a higher noise floor, coarser spatial resolution, more limited field of view, and/or longer averaging time than the quantum interferometry technique presented here. N-V–center spectroscopy leverages the unique capability of these optically active defect spins to act as nanoscale sensors directly integrated with the diamond crystal matrix, allowing strain measurements that are simultaneously fast, high-resolution, and sensitive.

The N-V center in diamond is a well-characterized [12,41,42] defect, currently used for many applications [5,6,43–45]. It is an $S = 1$ electronic system comprising a substitutional nitrogen impurity adjacent to a vacancy in the diamond carbon lattice. Figure 1(a) gives a simplified diagram of the N-V electronic and spin energy levels. Exposure to green light excites the electronic state into a phonon sideband; it decays quickly via the spontaneous emission of red fluorescence. Due to a differential

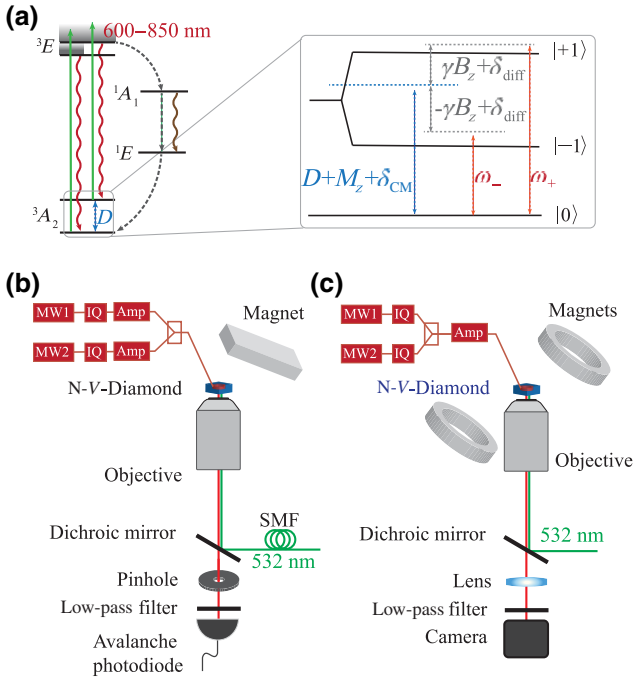

FIG. 1. (a) A simplified diagram of the N-V–center level structure. The detail shows the ground-state electronic spin energy levels, as well as the microwave (MW) field frequencies and detunings used in strain spectroscopy (additional details in text). (b),(c) The schematics of the confocal microscope and wide-field QDM used in this work (for additional details, see Appendices C and D).

coupling to an alternative decay path, the fluorescence intensity depends on the N-V spin state and there is preferential decay to the $m_S = 0$ sublevel. In addition, the N-V electronic spin can have long coherence lifetimes (microseconds to milliseconds) under ambient conditions. These key properties enable optical initialization and readout of the N-V spin state, allowing fast high-precision sensing of the environmental parameters that shift the N-V spin sublevels, including magnetic fields [2–4], strain [16,20,21], and temperature [46–48].

The axis between the nitrogen and vacancy that make up a N-V can be parallel to one of four crystallographic axes in the diamond crystal, creating four possible N-V classes that are typically equally populated in a N-V ensemble. When a bias magnetic field B_z is aligned with one of these N-V classes, the N-V ground-state spin Hamiltonian for that class reduces to [16]:

$$H = (D + M_z)S_z^2 + \gamma B_z S_z, \tag{1}$$

where D is the temperature-dependent zero-field splitting and M_z is the axial-stress-induced energy shift. The detail of Fig. 1(a) shows this ground-state energy-level structure, together with the microwave (MW) frequencies used to probe the N-V spin transitions. (Note that there is also hyperfine structure associated with these N-V energy levels, which is not indicated in Fig. 1.)

Previous diamond strain measurements using N-V centers have been performed via continuous wave (cw) [16,21,29,30] or pulsed [20] optically detected magnetic resonance (ODMR)—a simple robust technique where laser and MW fields are applied to the diamond and the MW frequency is swept or modulated. When the MW drive is resonant with the $|0\rangle \rightarrow |\pm 1\rangle$ spin transitions, the output N-V fluorescence decreases as the population transfers between spin states. (A more detailed discussion of cw ODMR, including measurements with this technique of the diamond used in this work, is included in Appendix F.)

III. STRAIN MEASUREMENTS USING QUANTUM INTERFEROMETRY

We achieve a 2-order-of-magnitude improvement in diamond strain sensitivity over previous work by overcoming two limitations of cw ODMR. First, we perform a Ramsey interferometric measurement, applying temporally separated pulsed MW fields to measure the phase acquired by the N-V spins during a free-evolution period. This avoids spectral broadening induced by the MW fields and fully leverages the quantum coherence of the N-V center [7,49]. (We note that pulsed ODMR also avoids this spectral broadening; however, it is in turn subject to other sensitivity-reducing effects, including Fourier broadening and inefficient hyperfine driving. For a detailed comparison of pulsed ODMR and Ramsey interferometric measurements, see Ref. [7].)

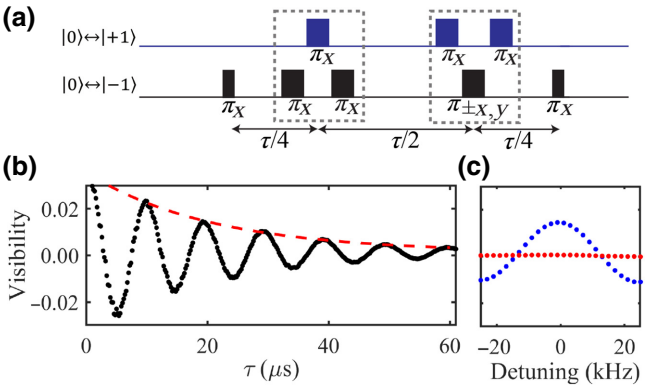

FIG. 2. (a) The timing diagram of MW pulses applied during a strain-CPMG measurement. (b) The strain-CPMG measurement of the N-V–ensemble visibility ν [defined in Eq. (3)] as a function of the evolution time, for MW detuning $\delta_{\mathrm{CM}} \approx 0.1$ MHz (see text for details). The red dashed line gives the decay envelope, with amplitude $Ae^{-\tau/T_D}$ (see text). The strain-CPMG dephasing time T_D is 21 μs, compared to the canonical inhomogeneous dephasing time $T_2^\star = 7.5$ μs measured using a Ramsey sequence (see Appendix B). (c) Calibration curves for fixed evolution time $\tau_1 = 21$ μs, showing ν as a function of the applied detunings δ_{CM} (blue, calibrating strain- or temperature-induced shifts in D) and δ_{diff} (red, calibrating magnetic field variation).

Second, we employ a variation on the Carr-Purcell-Meiboom-Gill (CPMG) spin-control sequence that is optimized for N-V–ensemble strain sensing: strain-CPMG, as shown in Fig. 2(a). The phase acquired during this sequence depends on M_z but is leading-order insensitive to magnetic inhomogeneity due to impurity spins—the leading source of dephasing for N-V ensembles in low-strain diamond [50]. The strain-CPMG sequence [47,51,52], and other magnetic-field-insensitive sequences [48,53], have been used for single–N-V thermometry but have not previously been used with N-V ensembles or to measure diamond strain.

A strain-sensitive, magnetic-field-insensitive measurement protocol is possible because the strain term in the Hamiltonian with an aligned bias magnetic field, given in Eq. (1), is quadratic in S_z, while the magnetic field term is linear. The need for an axial bias field, to maintain this distinguishability, limits such a protocol to measuring M_z for one N-V class at a time, which is assumed to result from a linear combination of normal strain along the three principal axes of the coordinate system of the N-V [28]. Such a single–N-V–orientation measurement satisfies many applications that require only the position and magnitude of strains and strain features, including optimization of nanostructure fabrication [19], strain probes in diamond cells and amorphous solids [29,30], failure analysis of diamond devices, and particle detection [32]. In applications

where additional information about the strain tensor is beneficial, the magnetic field could be realigned to measure M_z for all four N-V classes. This would allow reconstruction of components of the strain tensor [16], at the cost of a factor of 2 in sensitivity.

In a strain-CPMG measurement, we address the N-V spins with a pulsed MW field employing two tones near the two ground-state spin-transition frequencies, as illustrated in Fig. 1(a). Because the S_z and S_z^2 Hamiltonian terms respectively yield differential and common-mode shifts in the $|\pm1\rangle$ spin energy levels, we express the MW drive frequencies in terms of these shifts together with differential and common-mode detunings: $\omega_\pm = D + M_z + \delta_{\mathrm{CM}} \pm (\gamma B + \delta_{\mathrm{diff}})$. An initial $\pi/2$ pulse on the $|0\rangle \rightarrow |-1\rangle$ transition prepares the N-V electronic spins in an equal superposition of those states, which accumulates phase at a rate proportional to $(D + M_z) - \gamma B_z$. Triplets of π pulses swap the $|-1\rangle$ population into $|+1\rangle$, giving a superposition that accumulates phase proportional to $(D + M_z) + \gamma B_z$ (for further discussion of the swap pulses, see Appendix A). Over a full strain-CPMG sequence, with an even number of such swaps, the total B-dependent phase sums to zero and the final phase depends only on $D + M_z$. Similarly, the phase difference due to the differential detuning terms $\pm\delta_{\mathrm{diff}}$ also sums to zero, while the δ_{CM} terms add constructively; a final $\pi/2$ pulse encodes the phase difference acquired from the common-mode detuning δ_{CM} into the population of the $|0\rangle$ state, which can be read out via spin-dependent fluorescence.

The antisymmetric order of π pulses within the swaps is chosen to cancel out phase acquired due to pulse imperfections and the nonzero π-pulse duration [47]. Alternating the phase of one MW tone in the final swap operation changes the axis of rotation of that swap, allowing us to choose $\pm X$ or $\pm Y$ as the overall phase of the sequence (in the rotating frame).

The N-V–ensemble fluorescence measured after a strain-CPMG sequence with free-evolution time τ has the form

$$\begin{aligned} f_X^{\pm} &= f_i[1 \pm Ae^{-\tau/T_D} \sin(2\pi\delta_{\mathrm{CM}}\tau + \phi_0)], \\ f_Y^{\pm} &= f_i[1 \pm Ae^{-\tau/T_D} \cos(2\pi\delta_{\mathrm{CM}}\tau + \phi_0)], \end{aligned} \tag{2}$$

for a rotation around $\pm X$ or $\pm Y$. Here, A is the measurement contrast, T_D is the strain-CPMG dephasing time, and f_i is the fluorescence from the unpolarized N-V ensemble, all of which depend on the diamond material properties and the technical details of the apparatus [7]. δ_{CM} is the common-mode detuning for both MW tones, and ϕ_0 is a constant phase offset acquired during the drive and swap MW pulses. To normalize for fluctuations in laser power during a measurement, which affect f_i, we interlace strain-CPMG sequences with opposite overall phase (alternating between $+X$ and $-X$) and extract the interferometric visibility ν:

$$\nu = \frac{f_X^+ - f_X^-}{f_X^+ + f_X^-} = Ae^{-\tau/T_D} \sin(2\pi\delta_{\mathrm{CM}}\tau + \phi_0). \tag{3}$$

A measurement of ν versus the phase evolution time τ is shown in Fig. 2(b).

To convert ν to a measurement of M_z, we measure a calibration curve such as that shown in Fig. 2(c). We vary the common-mode MW detuning δ_{CM} by sweeping both drive tones in the same direction (e.g., low to high frequency) while keeping a fixed evolution time τ_1; this affects the fluorescence in the same way as a strain-induced change in M_z, giving an oscillation with period $1/\tau_1$ and amplitude $Ae^{-\tau_1/T_D}$. Figure 2(c) also shows a calibration for the differential detuning δ_{diff}, where sweeping the two drive tones in opposite directions is equivalent to a change in the magnetic field strength. Because δ_{diff} and the magnetic-field-induced precession cancel in the strain-CPMG sequence, this differential sweep has little effect on ν.

If the interference-fringe amplitude $Ae^{-\tau_1/T_D}$ is constant, then comparing the difference in visibility ν as measured at different spatial positions to a calibration curve gives a map of M_z (see below for a measurement protocol when this amplitude is not constant). To convert this frequency measurement into strain, we follow Ref. [28] in expressing M_z as a linear combination of normal strain:

$$M_z = A_1\epsilon_{zz} + A_2(\epsilon_{xx} + \epsilon_{yy}). \tag{4}$$

We use the pure strain convention, common in previous N-V–diamond strain measurements [20,54], which gives coupling constants $A_1 = -8.0(5.7)$ GHz per strain and $A_2 = -12.4(4.7)$ GHz per strain [28]. For a quantitative evaluation of sensitivity to arbitrary strains, we take a weighted average and obtain $\bar{\epsilon} = -M_z/(10.9(5.0)$ GHz per strain).

As this procedure measures $D + M_z$ without distinguishing between the sample- and temperature-dependent D and the strain shift M_z, it is best suited to measuring relative strain within a sample. Diamond is an outstanding thermal conductor [55], so D can be considered uniform across the millimeter-scale sample [51], while M_z will be constant in time unless we apply an external stress. We therefore interpret spatially differing measurements as revealing relative strain, whereas temporally differing measurements indicate changes in temperature. One further limit is that a measurement at evolution time τ_1 only determines the phase accumulated up to a factor of 2π; additional measurements at shorter evolution times can resolve this ambiguity but for the material used in this study, we find the strain variation to be within the dynamic range of a single τ value.

IV. EXPERIMENTAL DEMONSTRATIONS OF INTERFEROMETRIC STRAIN MICROSCOPY

We first implement the strain-CPMG protocol on diamond section A (see Appendix B) using a confocal scanning laser microscope [illustrated in Fig. 1(b)—see also Appendix C] to quantitatively evaluate the achievable strain sensitivity. We evaluate the measurement precision as a function of the averaging time via the Allan deviation [56], with the results shown in Fig. 3(b). From this procedure, together with the measured confocal volume of 0.54(2) μm^3, we obtain a volume-normalized strain sensitivity of $5(2) \times 10^{-8}/\sqrt{\text{Hz}\,\mu\text{m}^{-3}}$. The measurement stability is limited by shot noise in the avalanche-photodiode (APD) measurements of the N-V fluorescence; despite experimental imperfections, we obtain a sensitivity within 18% of the calculated shot-noise limit (see Appendix E). The dominant uncertainty in this measurement of strain sensitivity is the systematic uncertainty in the spin-strain coupling coefficients (discussed above). Other sources of uncertainty, including statistical uncertainty in the measured Allan deviations, uncertainty in the calibration curve fit used to convert visibility v to frequency shift M_z, and uncertainty in the measured confocal volume, each contribute at the level of approximately 1×10^{-9}.

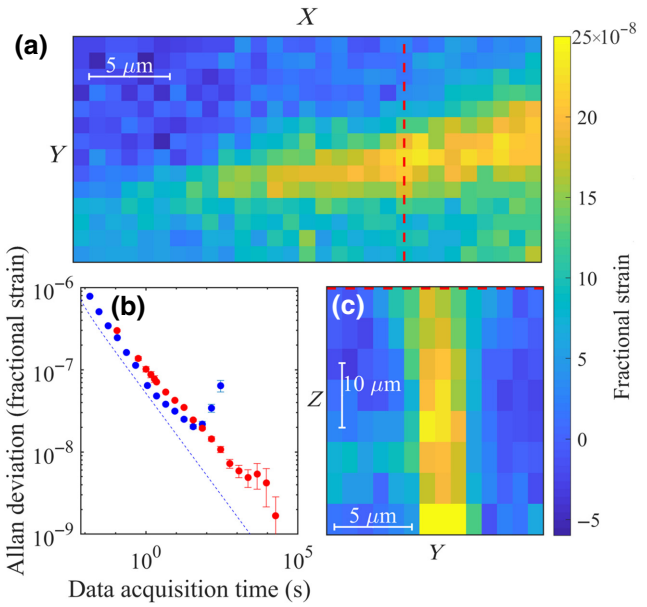

FIG. 3. Three-dimensional N-V–diamond strain measurements with a confocal scanning microscope. (a) The strain structure measured at the diamond surface. The position of the slice in (c) is marked with a red dashed line. (b) The Allan deviation for confocal strain measurements. The blue points are for single-position measurements, while the red points are for the "gradiometry" configuration (see text). The blue dotted line represents the calculated limit from shot noise in the avalanche photodiode (APD) used to measure N-V fluorescence (for details, see Appendix E). (c) An orthogonal slice across the strain feature, scanning beneath the diamond surface (marked by a red dashed line). The spatial scales are unequal due to the high index of refraction of diamond.

For measurement times greater than 20–30 s, determination of the visibility v is limited by variation in the diamond temperature of approximately 0.1 K/h, due to drifts in the laboratory temperature. We therefore also measure using a "gradiometry" configuration, in which measurements alternate between the scan position and a reference position on the diamond surface (arbitrarily chosen for each scan); the MW drive frequency is servoed on the reference measurement to compensate for thermal drift and preserve optimal sensitivity. This protocol costs a factor of approximately $\sqrt{2}$ in sensitivity relative to a single-position protocol, due to the time spent making reference measurements. However, it is stable for averaging times approaching 10^5 s, allowing scanning strain measurements to achieve high precision without effort to control external temperatures beyond that in a typical laboratory environment. The Allan deviation of a series of measurements in this configuration is also shown in Fig. 3(b).

Figure 3 also shows two slices of a strain map produced by confocal scans across a feature in the diamond sample. These measurements use the gradiometry configuration to counteract temperature drift during the scans, which require approximately 6 h each. Figure 3(a) shows a map obtained by scanning across the surface of the diamond, while Fig. 3(c) shows an orthogonal slice taken by scanning into the diamond. As the feature's strain magnitude grows and its spatial extent shrinks with increasing depth of the confocal spot beneath the diamond surface, it may result from a scratch or extended crystallographic defect originating at or near the opposite surface of the diamond.

When scanning at multiple depths below the diamond surface, as during the acquisition of Fig. 3(c), the visibility v cannot be converted to a measurement of M_z by a single calibration curve, as the amplitude of the driving field from the planar MW loop falls off with depth, reducing the interference-fringe amplitude $Ae^{-\tau_1/T_D}$. We therefore measure what we term the "XY-normalized" visibility v_{XY}:

$$v_{XY} = \frac{f_X^+ - f_X^-}{\sqrt{(f_X^+ - f_X^-)^2 + (f_Y^+ - f_Y^-)^2}}. \tag{5}$$

In addition to fluctuations in laser power, this quantity is also normalized against fluctuations in the interference-fringe amplitude. From Eq. (2) we obtain

$$\sqrt{(f_X^+ - f_X^-)^2 + (f_Y^+ - f_Y^-)^2} = 2f_i A e^{-\tau_1/T_D}, \tag{6}$$

which together with Eq. (5) gives

$$v_{XY} = \sin(2\pi\delta_{\text{CM}}\tau + \phi_0). \tag{7}$$

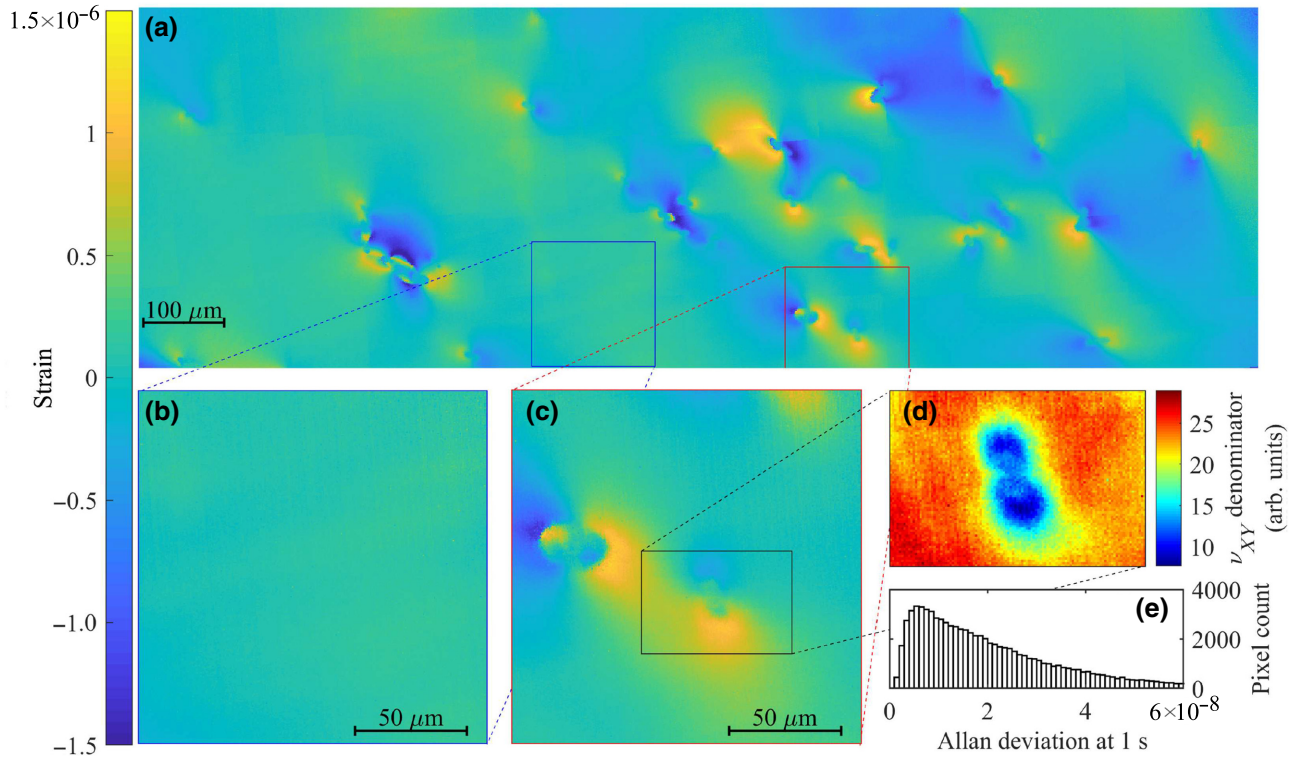

FIG. 4. Wide-field strain images taken with a QDM. (a) A wide survey of the strain features on diamond section B. Individual fields of view, each representing about 150 × 150 μm^2 and 1 s of data acquisition, are manually stitched together by aligning overlapping features to form a composite image; minor compositing artifacts result from temperature drift between image acquisitions. (b),(c) Single fields of view, as measured in 1 s of data acquisition each. Panel (b) features extremely homogeneous strain, characteristic of this diamond material. Panel (c) showcases two strain features, likely induced by crystallographic defects incorporated during CVD growth. (d) The denominator of the XY-normalized visibility indicates areas where intrapixel strain gradients degrade the dephasing time T_D (see text). (e) A histogram of the Allan deviations for 1 s of data acquisition for each pixel in (b), giving an estimate of the strain measurement uncertainty.

As a result, no amplitude calibration is required to extract M_z from ν_{XY}. The measurement of X and Y quadratures costs a factor of $\sqrt{2}$ in sensitivity for a fixed overall measurement time; but the only cost from MW inhomogeneity is increased statistical uncertainty for positions with smaller $Ae^{-\tau_1/T_D}$, rather than erroneous systematic shifts in the measured strain. The robustness of the XY-normalized technique is especially useful for wide-field strain imaging (described below), where laser and MW power inhomogeneity can be significant [57].

While confocal scanning microscopy allows strain mapping in three dimensions with a well-defined interrogation volume, many applications benefit from the speed and scalability of wide-field imaging. For example, diamond characterization and engineering require broad surveys of millimeter-scale diamond to understand the overall growth properties [13,33]; nanofabrication analysis could benefit from the measurement of many devices in parallel [19]; and dark-matter detection will require the rapid analysis of large volumes of material to find particle impact sites [32]. We therefore implement wide-field N-V–diamond strain imaging on diamond section B (see Appendix B) using a QDM, schematically illustrated in Fig. 1(c) (see also Appendix D). This QDM uses a Heliotis heliCam™ lock-in camera, described in detail in Ref. [58], to quickly acquire N-V fluorescence images. Figure 4 shows wide-field images of strain across a region of the diamond material. Figure 4(a) presents a broad survey comprising many individual fields of view, while Figs. 4(b) and 4(c) show single fields of view after 1 s of data acquisition. Figure 4(b) demonstrates the sensitive measurement of a typical low-strain region on the sample, while Fig. 4(c) shows the capability to image strain features of interest.

In addition to preventing systematic shifts due to laser and MW power inhomogeneity, the measurement of ν_{XY} resolves a second problem that is more pronounced with a QDM than with a confocal microscope: strain gradients within a single pixel. These gradients can be very large at the edges or centers of strain features, meaning that measurement of the mean strain-induced frequency shift within a pixel may not adequately encode the strain structure. Worse, gradients within a pixel yield a

distribution of different precession frequencies, causing dephasing and reducing T_D compared to low-gradient pixels—potentially "washing out" the average strain shift and leading to noisy or misestimated strain readout. However, the denominator of v_{XY} is proportional to $e^{-\tau_1/T_D}$ and therefore can be used as a signal identifying such high-gradient pixels. Figure 4(d) shows an example of this effect; the interference-fringe amplitude $Ae^{-\tau_1/T_D}$ is reduced to approximately $1/e$ of the value for nearby low-strain regions—consistent with an additional strain gradient of about 1.4×10^{-6} within the volume and an attendant decrease in dephasing time from about 20 to 10 μs.

Figure 4(e) shows a histogram of 1-s Allan deviations for pixels in the low-strain QDM image, Fig. 4(b). The sensitivity variation is largely due to inhomogeneity of approximately 60% in the green excitation laser power across the field of view—lower laser power implies larger fractional shot noise, due to the collection of fewer fluorescence photons. Additionally, laser inhomogeneity can lead to reduced contrast A in some regions, if the optical power is insufficient to fully repolarize the N-V centers between strain-CPMG measurements.

Lacking depth restriction smaller than the focal plane of the 20× microscope objective used with the QDM, each pixel in the imaging field of view integrates light from a larger diamond volume than the confocal spot; Fig. 4(e) demonstrates the (non-volume-normalized) strain sensitivity achievable with this greater integration volume. For diamond-engineering applications requiring broad surveys of material (but not demanding the higher spatial resolution offered by the confocal method), the wide field of view and high sensitivity of the QDM, demonstrated in Fig. 4, are significant advantages. Additionally, the resilience of the strain-CPMG sequence to nuclear-spin-bath-induced magnetic inhomogeneity will allow sensitive strain characterization in diamonds with high nitrogen or ^{13}C content, which is currently limited by broad ODMR line widths and short dephasing times. Future work toward other applications, such as photonic structure engineering and dark-matter searches, will implement improved depth resolution in wide-field imaging, e.g., using structured illumination or light-sheet microscopy [32]; and for each resulting μm^3-scale pixel in a QDM image, we expect the strain sensitivity to be similar to that measured with the confocal technique.

V. CONCLUSION

In conclusion, we demonstrate diamond crystal-strain measurement with a volume-normalized sensitivity of $5(2) \times 10^{-8}/\sqrt{(\text{Hz}\ \mu\text{m}^{-3})}$–a 2-order-of-magnitude improvement over previous work [16] – achieved via magnetic-field-insensitive quantum interferometry on an ensemble of N-V centers. Measurements with a confocal scanning microscope allow three-dimensional strain mapping with micron-scale spatial resolution, as well as quantitative characterization of the volume-normalized sensitivity. Such a scanning protocol could enable sensitive *in situ* measurements of strain in diamonds embedded in transparent materials or anvil cells. The protocol also exceeds the sensitivity benchmark of $10^{-7}/\sqrt{\text{Hz}\ \mu\text{m}^{-3}}$ for the detection of particle-induced crystal damage in a directional search for WIMP dark matter [32]. Measurements with a wide-field-imaging QDM demonstrate speed and field of view that also surpasses a benchmark of $(125 \times 125)\ \mu\text{m}^2/\text{s}$ for the proposed future dark-matter detector [32]. Beyond this basic physics application, wide-field diamond strain imaging as demonstrated here will enable sensitive surveys of strain features for diamond engineering, as well as improved characterization of diamond nanofabrication for quantum and other devices. In particular, short N-V electronic spin dephasing times currently inhibit sensitive strain characterization in diamonds with high nitrogen or ^{13}C content, which are used for many scientific and industrial applications, including diamond knives and anvil cells. The quantum interferometry technique is less sensitive to such sources of N-V spin dephasing; it could therefore help to improve production and characterization of these and other diamond devices beyond high-purity CVD samples.

We note that the sensitivity of the confocal scanning measurements could be further enhanced with improvements to low-light detection by replacing the avalanche photodiode with (for example) a multipixel photon counter array; while future work will improve wide-field imaging by increasing depth resolution. Additionally, the strain sensitivity in both the confocal and QDM configurations could be further enhanced with improvements in diamond material, if the N-V density can be increased without compromising a long strain-CPMG dephasing time T_D.

ACKNOWLEDGMENTS

This work was supported by the U.S. Department of Energy (DOE) "Quantum Information Science Enabled Discovery" (QuANTISED) program under Award No. DE-SC0019396; the Army Research Laboratory Maryland-ARL Quantum Partnership program under Contract No. W911NF-19-2-0181; the Defense Advanced Research Projects Agency (DARPA) "Driven and Nonequilibrium Quantum Systems" (DRINQS) program under Grant No. D18AC00033; the DOE fusion program under Award No. DE-SC0021654; and the University of Maryland Quantum Technology Center. This work was performed in part at the Harvard Center for Nanoscale Systems (CNS), a member of the National Nanotechnology Coordinated Infrastructure Network (NNCI), which is supported by the

National Science Foundation (NSF) under NSF Award No. 1541959.

APPENDIX A: INTERFEROMETRIC STRAIN SENSING PROTOCOL

A schematic of the N-V–diamond strain Carr-Purcell-Meiboom-Gill (strain-CPMG) sensing protocol is shown in Fig. 5(a). First, green laser illumination prepares the N-V–ensemble ground-state spins in the $|m_s = 0\rangle$ state. Then, a MW $\pi/2$ pulse resonant with the $|0\rangle \rightarrow |-1\rangle$ transition prepares the N-V ensemble in an equal superposition of the $|0\rangle$ and $|-1\rangle$ states. During the subsequent free-evolution time [illustrated by red traces in the lower panel of Fig. 5(a)], the N-V spins accumulate a relative phase with the rate $D + M_z - \gamma B_z$, where these parameters are defined in the main text in the context of the N-V spin Hamiltonian. Next, triplets of MW π pulses collectively swap the N-Vs between the $|-1\rangle$ and $|+1\rangle$ states (see below for more details). Thus, during the subsequent free-evolution time, the phase accumulation rate is $D + M_z + \gamma B_z$. Dividing the total free-evolution time evenly between the $|+1\rangle$ and $|-1\rangle$ states yields a final accumulated N-V phase independent of B_z in a form of balanced spin-state interferometry designed to be exclusively sensitive to $D + M_z$. The final $\pi/2$ pulse converts the accumulated phase into a fractional N-V population in $|0\rangle$ and $|-1\rangle$, which is read out via state-dependent fluorescence.

1. Time evolution during swap pulse

During the strain-CPMG sequence, triplets of MW π pulses collectively swap the N-V population between the $|-1\rangle$ and $|+1\rangle$ states [see Fig. 5(a)]. In this appendix, we calculate the time evolution of an arbitrary initial state during the swap operation. To demonstrate the dynamics of the swap operation, we derive an analytic solution for the ideal case of resonant MW drive fields; the more general case of driving with detunings must be treated numerically [59]. The N-V spin Hamiltonian under resonant MW driving is

$$H = (D + M_z)S_z^2 + \gamma B S_z + [\gamma B_+ \cos(\omega_+ t + \Delta\phi_+) + \gamma B_- \cos(\omega_- t + \Delta\phi_-)]S_x, \tag{A1}$$

where $\omega_\pm \equiv D + M_z \pm \gamma B$, $B_\pm$, and $\Delta\phi_\pm$ are the frequencies, amplitudes, and phases of the applied MW fields. After performing a unitary transformation $V = \mathrm{diag}(e^{-i\omega_+}, 1, e^{-i\omega_-})$ into a frame rotating with the MW

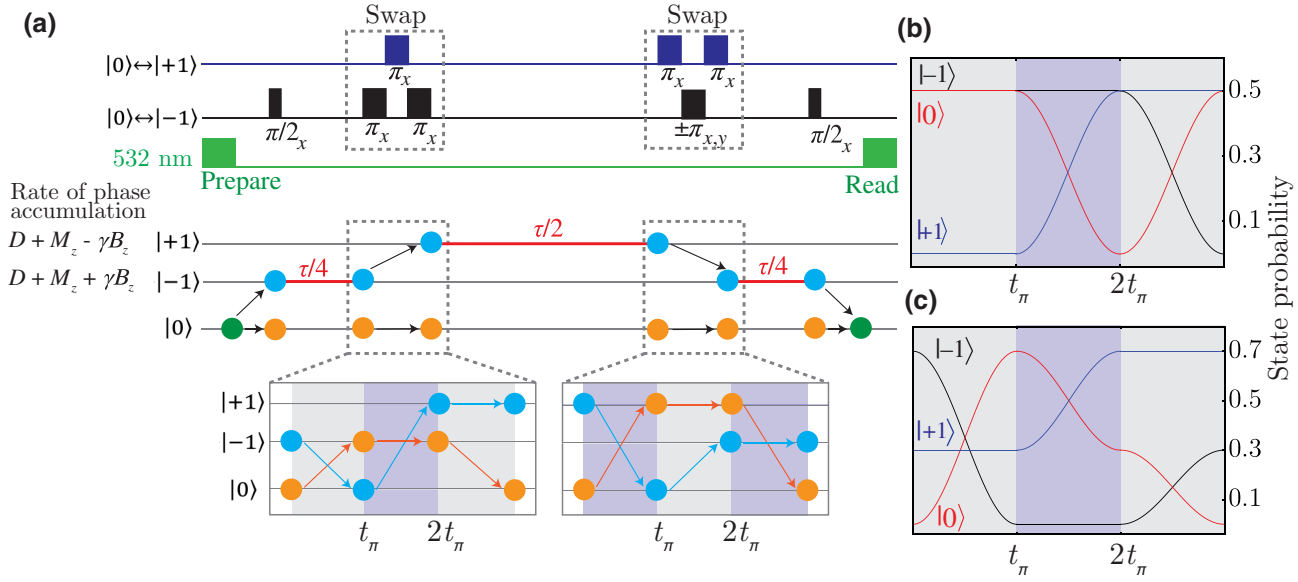

FIG. 5. (a) The detailed schematics of the strain-CPMG interferometric sensing protocol. Top: the strain-CPMG pulse sequence. Bottom: the N-V spin population in each of the $|m_s = 0, \pm 1\rangle$ states as a function of time. The swap operation exchanges the population between $|+1\rangle$ and $|-1\rangle$ states. Free-evolution intervals are highlighted in red. The insets schematically illustrate the evolution of the N-V spin-state populations during swap operations. The first laser pulse initializes the N-Vs into $|0\rangle$, while the final laser pulse reads out the state-dependent fluorescence. (b),(c) The time evolution of the state populations under the swap operation, using Eq. (A3). The gray and blue shaded areas show the evolution under resonant MW fields addressing the $|0\rangle \leftrightarrow |-1\rangle$ and $|0\rangle \leftrightarrow |+1\rangle$ transitions, respectively. (b) The analytical calculation of the time course of the N-V spin-state populations undergoing the strain-CPMG protocol, for an initial condition chosen such that the N-V spin-state populations are equally separated between $|0\rangle$ and $|-1\rangle$, similar to an ideal case for the first swap pulse in the experiment. (c) The analytical calculation for an arbitrary initial condition with 70% of the N-V population in $|-1\rangle$ and 30% in $|+1\rangle$, such that the nonequal populations at each step better illustrate the dynamics under the swap pulses.

drive fields and dropping rapidly oscillating terms, this system can be solved analytically. The evolution operator in the transformed frame is then

$$U(B_{\pm},\Delta\phi_{\pm};t)=\begin{pmatrix} \frac{B_-^2+B_+^2\cos(\omega_e t)}{B_+^2+B_-^2} & \frac{-iB_+e^{-i\Delta\phi_1}\sin(\omega_e t)}{\sqrt{B_+^2+B_-^2}} & \frac{[-1+\cos(\omega_e t)]B_+B_-e^{-i(\Delta\phi_1-\Delta\phi_2)}}{B_+^2+B_-^2} \\ \frac{-iB_+e^{-i\Delta\phi_1}\sin(\omega_e t)}{\sqrt{B_+^2+B_-^2}} & \cos(\omega_2 t) & \frac{-iB_-e^{-i\Delta\phi_2}\sin(\omega_e t)}{\sqrt{B_+^2+B_-^2}} \\ \frac{[-1+\cos(\omega_e t)]B_+B_-e^{-i(\Delta\phi_1-\Delta\phi_2)}}{B_+^2+B_-^2} & \frac{-iB_-e^{-i\Delta\phi_2}\sin(\omega_e t)}{\sqrt{B_+^2+B_-^2}} & \frac{B_+^2+B_-^2\cos(\omega_e t)}{B_+^2+B_-^2} \end{pmatrix}, \tag{A2}$$

where $\omega_e \equiv (\gamma/2\sqrt{2})\sqrt{B_+^2+B_-^2}$ [59]. After solving the evolution of an initial state $|\tilde{\psi}(0)\rangle$ in the transformed frame, we transform the state back to the laboratory frame: $|\psi\rangle_{\rm lab} = V|\tilde{\psi}\rangle$. For a detailed derivation of the evolution operator, refer to Ref. [59]; for an alternative discussion of strain-CPMG swap pulses, see Ref. [47].

We construct the state evolution under the first swap operation in Fig. 5(a) (i.e., swap from $|-1\rangle$ to $|+1\rangle$) using the evolution operator:

$$U_{\rm swap}(t)=\begin{cases} U(B_-{=}1,B_+{=}0,\Delta\phi_{\pm}{=}0;0<t<t_\pi), \\ U(B_-{=}0,B_+{=}1,\Delta\phi_{\pm}{=}0;t_\pi<t<2t_\pi), \\ U(B_-{=}1,B_+{=}0,\Delta\phi_{\pm}{=}0;2t_\pi<t<3t_\pi). \end{cases} \tag{A3}$$

Figure 5(b) shows the population in each state as a function of time during these swap pulses, for an ideal strain-CPMG measurement, while Fig. 5(c) shows the time evolution for an arbitrary initial state under $U_{\rm swap}(t)$, to better illustrate the full swap dynamics with unequal populations.

2. Strain-CPMG with $N > 2$ swap pulses

We measure the strain-CPMG dephasing time T_D using strain-CPMG sequences with increasing numbers of swap operations. While strain-CPMG sequences cancel phase accumulated due to magnetic fields that are static or slowly varying over the time scale of the sequence, these sequences remain vulnerable to higher-frequency magnetic noise (e.g., dephasing induced by electronic or nuclear-spin-bath dynamics). In the absence of all other contributions, T_D would therefore be expected to approach the ensemble decoherence time (T_2) and to increase with additional swap operations. However, as shown in Figs. 6(a)–6(c),T_D is largely independent of the number of swap operations applied and shorter than even the Hahn-echo $T_2 \approx 100$ μs observed in this diamond. This suggests that T_D for the two-swap sequence (and sequences with an increasing number of swap operations) is dominated by inhomogeneous common-mode shifts, effects that the strain-CPMG sequence is designed to preserve—for example, inhomogeneous strain distributions within a confocal spot or camera pixel, potentially arising from microscopic variations in the distribution of nitrogen or other impurities near each N-V center. Meanwhile, as demonstrated by the decreasing interference-fringe amplitude A in Figs. 6(a)–6(c), increasing numbers of swap operations allow small MW pulse errors to accumulate, reducing measurement contrast; the measurements in this work are therefore performed using a strain-CPMG sequence with two swap operations.

APPENDIX B: COMPARISON OF DEPHASING TIMES

The single-crystal bulk diamond material used in this work is grown by Element Six, Ltd., via {100} CVD employing isotopically purified ^{12}C enriched with nitrogen. After growth, diamond sections A and B are cut

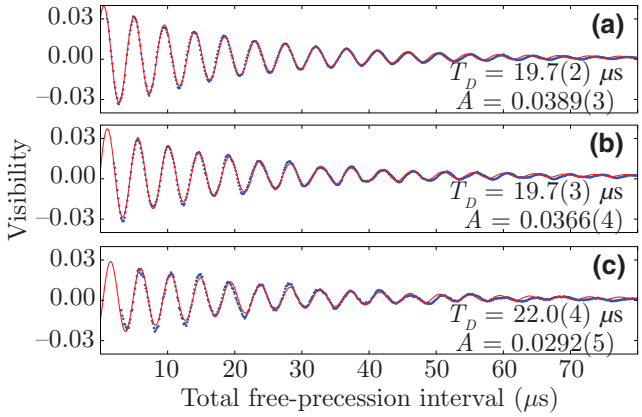

FIG. 6. A comparison of strain-CPMG sequences with different numbers of swap operations: time traces of the visibility v [see Eq. (3) below], with both MW tones detuned from resonance with a common-mode detuning $\delta_{\rm CM} = 0.35$ MHz, for (a) two-swap, (b) four-swap, and (c) six-swap strain-CPMG sequences. The blue data points are measured values, while the red curves are fits to an exponentially decaying sinusoid. The two resulting fit parameters that determine sensitivity, i.e., the amplitude A and the decay rate T_D, are quoted for each sequence. The initial lag for the first data point arises from the minimum initial delay between swap operations.

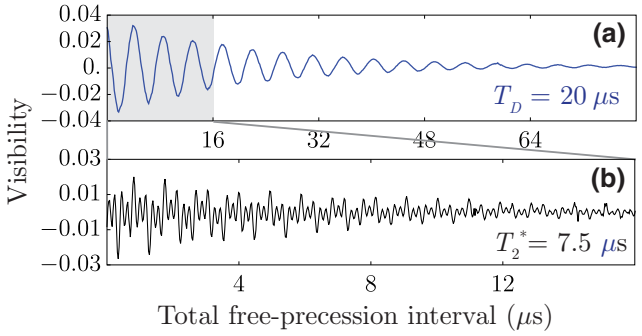

FIG. 7. A comparison of the free induction decays for different measurement protocols. (a) The visibility (v) as a function of the evolution time for the strain-CPMG sequence with common MW detuning $\delta_{CM} = 0.35$ MHz, yielding a determination of T_D. (b) SQ measurement, addressing the $|0\rangle \leftrightarrow |+1\rangle$ transition with 3-MHz detuning, providing a determination of T_2^*. The visibility oscillates as a superposition of three frequencies, each of which are detunings from hyperfine splittings. The SQ-measurement result is shown for the first 16 μs, addressing the same period as that shown in the gray-shaded region in (a) for the strain-CPMG measurement result.

from the material and separately electron irradiated and annealed, forming N-V centers with an estimated [N-V] density of 0.3 ppm in section A (used for confocal measurements) and 0.5 ppm in section B (used for wide-field imaging). The resulting octagonal diamond chips have dimensions of $3.4 \times 3.4 \times 0.1$ mm^3 and feature relatively homogeneous crystal strain (see Fig. 4 of the main text). Both diamond sections have a similar ensemble N-V inhomogeneous dephasing time $T_2^* \approx 7.5\ \mu$s and strain-CPMG dephasing time $T_D \approx 20\ \mu$s.

In addition to the strain-CPMG dephasing time T_D [discussed in the main text and shown in Fig. 7(a)], we also measure the inhomogeneous dephasing time T_2^* using a standard single-quantum (SQ) Ramsey measurement protocol [7]. This protocol treats the N-V ground-state spin as an effective spin-1/2 system, only addressing one of the two transitions $|0\rangle \leftrightarrow |+1\rangle$ or $|0\rangle \leftrightarrow |-1\rangle$ (which are split by the applied magnetic bias field). Figure 7 shows measured visibility free-induction decays for the strain-CPMG and Ramsey protocols. The three frequencies visible in the Ramsey curve correspond to drive detunings from each of the three hyperfine levels; these three frequencies are not present in the strain-CPMG measurement because the hyperfine splitting arises from an effective magnetic field and cancels under that protocol. This comparison clearly demonstrates the enhanced dephasing time attained with strain-CPMG compared to a standard Ramsey measurement.

APPENDIX C: CONFOCAL MICROSCOPE

For the confocal measurements reported in this work, we use a custom-built confocal scanning laser microscope optimized for N-V spin-state manipulation and optical measurements. A diode-pumped solid-state laser provides 10 mW of 532-nm excitation light at maximum power, which is switched by an acousto-optic modulator (AOM) and spatially filtered by a polarization-maintaining single-mode fiber (SMF). (The signal-to-noise ratio for N-V spin-state determination continues to improve up to the maximum available power.) This light is reflected by a dichroic mirror into the aperture of a microscope objective (Olympus, 100× magnification, 0.9 NA air) and focused into the diamond sample, which is held on a nanopositioning stage. Red fluorescence from the N-Vs is collected by the same objective and passes through the dichroic mirror into the collection optics. A pinhole spatially filters the fluorescence light, which is then focused onto an APD operating in linear mode. MW control of the N-V spins is provided by two MW signal generators, each coupled through a 16-W amplifier joined by a power combiner; the combined MW signal is broadcast to the N-Vs by an omega-loop antenna fabricated on a glass cover slip held in contact with the diamond sample. The MW- and laser-induced temperature change within each measurement cycle is negligible, but we do observe changes in the sample temperature on the order of tens of millikelvins as a function of the duty cycle; we control this effect by keeping the confocal duty cycle constant throughout all of the measurements reported here.

To quantitatively characterize the N-V ensemble within the diamond volume addressed by the confocal microscope and determine the volume-normalized strain sensitivity of the N-V ensemble, we measure the confocal point-spread function using a single N-V center, approximately 1 μm below the surface of a different diamond sample of similar geometry. For this measurement, we place a single-photon-counting module (SPCM) at the focus of the collection optics, switching between the SPCM and the APD by means of a flip mirror. A fit of the measured fluorescence distribution to a three-dimensional Gaussian function yields the confocal volume of 0.54(2) μm^3.

APPENDIX D: QDM WIDE-FIELD IMAGER USING heliCam C3 LOCK-IN CAMERA

For the wide-field imaging reported in this work, we use a QDM apparatus and a Heliotis heliCam C3 camera—both described in detail in Ref. [58]. The heliCam C3 subtracts alternating N-V fluorescence exposures in hardware and digitizes only their difference, allowing the measurement contrast to fill the 10-bit dynamic range of each pixel. The rate of these exposures is defined by a user-controlled demodulation signal at frequency f_{demod}; during one demodulation cycle, the camera takes four exposures and digitizes two difference images. The N_{demod} values of these cycles are accumulated and their average is sent to the computer. The typical values for this work

($N_{\text{demod}} = 24$ and $f_{\text{demod}} = 6.5$ kHz) give an external frame rate of approximately 270 Hz.

The heliCam adds an independent fixed pixel-by-pixel offset to each exposure in a demodulation cycle, likely arising from the different capacitor banks used to store the exposures for subtraction. In Ref. [58], this offset has been subtracted with a separate calibration measurement for each field of view on the diamond, in preparation to sense magnetic fields due to an additional sample signal. The strain-sensing applications addressed here typically require quickly imaging many diamond fields of view and preclude a full calibration measurement at each one. We therefore subtract out these offsets by taking the difference between two frames at drive frequencies on either side of a Ramsey fringe; we measure for 0.5 s at each frequency to give an overall 1-s data-acquisition time.

In contrast to the confocal measurements, we find no evidence of MW- or laser-induced heating in the QDM configuration. This is likely due to reduced thermal contact between the MW loop and the diamond sample in the QDM, where the MW loop is freestanding, compared to the confocal, where the MW loop is printed on a cover slip mounted directly against the sample surface.

We note that while the greater interrogation volume in the wide-field imaging setup demonstrated here improves measurement times for applications not requiring submicron spatial resolution, it necessarily implies reduced rejection of out-of-focus light compared to the confocal geometry. Wide-field diamond imaging thus brings with it the possibility of measurement contamination by collection of light that has internally reflected from elsewhere in the diamond. We see no evidence of this effect either in the measurements presented here or previous wide-field QDM measurements able to reliably resolve micron-scale magnetic or strain features [1,16,39,40,58,60]. In the current work, the imaging of high- and low-strain regions within microns of each other (as shown in Fig. 4 of the main text) indicates that optical measurement contamination, if present, is not significant enough to blur the sharp edges of strain features in the diamond sample.

APPENDIX E: NOISE LIMIT ON STRAIN SENSITIVITY

To determine the expected noise limit to sensitivity in the confocal measurements, we estimate the noise current and voltage from the APD and Johnson noise in the transimpedance amplifier, convert this estimated noise from voltage to visibility ν, and, finally, use a strain calibration curve to determine the shot-noise limit on our strain measurements.

For fluorescence detection in the confocal microscope, we use a Thorlabs APT410A APD-based photodetector. The rms noise current in an APD is given by

$$i_N = \sqrt{2q\left\{I_{\text{DS}} + \left[I_{\text{DB}}M^2 + R_0(\lambda)M^2P_s\right]F\right\}B}, \quad \text{(E1)}$$

where the first term is surface dark current, the second term is bulk leakage current, and the third term is photon shot noise from N-V fluorescence. Both the bulk leakage current and the photon shot noise are enhanced by the APD gain M and excess noise factor F. Additionally, q is the electron charge, $R_0(\lambda)$ is the APD responsivity at $M = 1$ for a given wavelength, P_s is the incident optical power onto the APD, and B is the measurement bandwidth.

The responsivity at $M = 100$ for 700 nm is approximately 45 A/W; combined with a transimpedance gain of 250 kV/A, the total gain is 11.25×10^6 V/W. A typical APD output voltage of 5.2 mV thus corresponds to fluorescence power $P_s = 0.46$ nW, giving $R_0(\lambda)M^2P_s \approx 0.21$ mA.

The typical noise-equivalent power (NEP) for the APD410A with no input light is specified as $0.04\,\text{pW}/\sqrt{\text{Hz}}$; cases where the entire NEP is due to surface or bulk dark current give upper limits of $I_{\text{DS}} \leq 200$ pA and $I_{\text{DB}} \leq 2$ pA (obtained by multiplying the NEP by the responsivity and by the gain if appropriate). These are each negligible compared to the photon-shot-noise term, even after accounting for the factor of M^2 in the bulk-dark-current term.

The excess noise factor for the APD410A is $F = 4$. Finally, we measure the data-acquisition- (DAQ) system bandwidth B to be 700 kHz, via the rise time of the APD response to a fast AOM pulse. (The AOM rise time is measured separately, with a high-power photodiode and fast oscilloscope, and shown to be significantly faster than the DAQ bandwidth.) Equation (E1) thus gives an expected rms noise current of $i_N = 1.4$ nA. The transimpedance gain of 250 kV/A then yields the estimated rms noise voltage:

$$v_{\text{SN}} = 0.34\ \text{mV}. \quad \text{(E2)}$$

The estimated rms Johnson-Nyquist noise in the transimpedance amplifier is given by $v_{\text{JN}} = \sqrt{4k_BTRB}$, where k_B is the Boltzmann constant, T is the temperature (approximately 300 K), R is the resistor value, and B is the bandwidth. The equivalent resistance of the transimpedance amplifier of the APD410A is 250 kΩ, resulting in an estimated rms Johnson-Nyquist noise of

$$v_{\text{JN}} = 0.05\ \text{mV}. \quad \text{(E3)}$$

v_{JN} adds in quadrature with v_{SN} and therefore is essentially negligible; the expected rms voltage noise is thus given by Eq. (E2). Digitization noise and error, respectively specified at 15 μV rms and 52 μV absolute accuracy for the NI PCIe-6251 DAQ used in this work, are also negligible compared to shot noise.

The uncertainty in the visibility $\nu = (f_X^+ - f_X^-)/(f_X^+ + f_X^-)$ is given by

$$\sigma(\nu) = \sqrt{\left(\frac{1-\nu}{f_X^+ + f_X^-}\right)^2 \sigma(f_X^+)^2 + \left(\frac{1+\nu}{f_X^+ + f_X^-}\right)^2 \sigma(f_X^-)^2}. \tag{E4}$$

Noting that $\nu \propto Ae^{-\tau_1/T_D} \sim \mathcal{O}(0.01) \ll 1$, we have

$$\sigma(\nu) \simeq \frac{\sqrt{\sigma(f_X^+)^2 + \sigma(f_X^-)^2}}{f_X^+ + f_X^-} = \frac{\sqrt{2}v_{\mathrm{SN}}}{f_X^+ + f_X^-} \approx 0.046. \tag{E5}$$

Conversion of this signal uncertainty to strain units using a fitted calibration curve [see Fig. 2(b) and associated discussion in the main text] gives an estimated noise limit on the strain sensitivity of $5.2 \times 10^{-8}/\sqrt{\mathrm{Hz}}$ [the blue dotted line in Fig. 3(b) of the main text]. This noise limit is approximately 18% smaller than the measured Allan deviation at 1 s shown in Fig. 2(b), $6.4(1) \times 10^{-8}$. The shot-noise calculation presented here is not normalized to the confocal spot size; assuming a square-root scaling with volume, the shot-noise limit and measured sensitivity are, respectively, 3.8 and $4.7(1) \times 10^{-8}/\sqrt{\mathrm{Hz}\ \mu\mathrm{m}^{-3}}$. Note that the uncertainty in the spin-strain coupling coefficient is common to both the shot-noise calculation and the measured sensitivity and does not affect the comparison between them.

APPENDIX F: cw ODMR STRAIN IMAGING

cw ODMR is a robust measurement method where cw laser and MW fields are applied to the diamond. When the MWs are off resonance, the green laser light polarizes the N-V–center electron spins into the $|0\rangle$ state, maximizing their fluorescence output. When the MWs are resonant with the ground-state spin transitions, they mix the $|0\rangle$ and $|+1\rangle$ or $|-1\rangle$ states, reducing the fluorescence. Sweeping the MW frequencies and monitoring the fluorescence allows determination of $|0\rangle \rightarrow |\pm 1\rangle$ transition frequencies.

The N-V ground-state spin Hamiltonian with a bias magnetic field $|\vec{B}| > 1$ mT, as used in this work, reduces to [16]

$$H_\kappa = (D + M_{z,\kappa})S_{z,\kappa}^2 + \gamma \vec{B} \cdot \vec{S}_\kappa, \tag{F1}$$

where $\kappa = (1, 2, 3, 4)$ represent the four possible classes of N-V centers pointing along four crystallographic directions [as shown in Fig. 8(a)].

As discussed in the main text, in this work we align the bias magnetic field with one of the four N-V classes, which enables separation of strain ($\propto S_z^2$) and magnetic field ($\propto S_z$) terms in the Hamiltonian for that N-V class. The three remaining N-V classes each therefore see equal magnetic field projections $\vec{B} \cdot \vec{S}$. Figure 8(c) shows an example cw ODMR spectrum under this condition, acquired during this work. The aligned N-V class sees an axial field $B_z \approx 2.1$ mT, while the projection onto each other class is $\vec{B} \cdot \vec{S} \approx 0.75$ mT. Each N-V class yields two dips in fluorescence in the spectrum, corresponding to the $|0\rangle \rightarrow |\pm 1\rangle$ spin transitions; each of these transitions is split into three lines by the hyperfine interaction with the spin-1 ^{14}N nucleus.

The transition frequencies for the aligned N-V class are

$$f_\pm = (D + M_z) \pm \gamma B_z, \tag{F2}$$

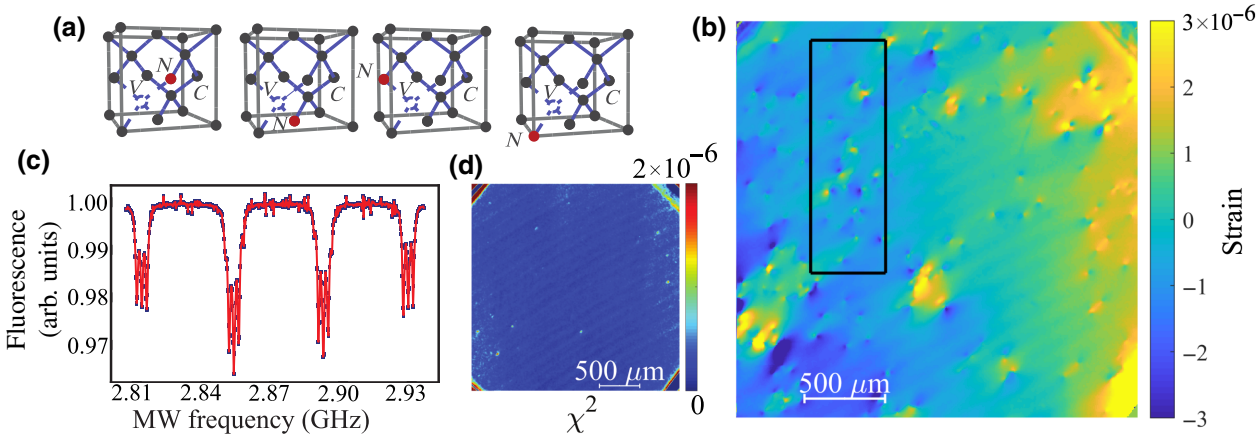

FIG. 8. (a) Four N-V orientation classes, pointing along four crystallographic directions in the diamond crystal lattice. (b) The wide-field strain map of diamond section B, acquired using methods and QDM apparatus described in Ref. [16]. The black rectangle designates the region shown in Fig. 4. (c) An example optically detected magnetic resonance (ODMR) spectrum from an N-V ensemble; changes in fluorescence intensity reveal spin-transition frequencies. Each N-V resonance, corresponding to one or more of the four N-V orientation classes, is split into three lines due to hyperfine interactions with the spin-1 ^{14}N nucleus. (d) A map of the χ^2 goodness-of-fit statistic for per-pixel fits, yielding the strain map of shown in (b). Large intrapixel strain gradients degrade the fits via deviation from Lorentzian line shapes.

where γ is the N-V gyromagnetic ratio. Measurement of both the $|0\rangle \rightarrow |-1\rangle$ and $|0\rangle \rightarrow |+1\rangle$ transitions allows separation of the frequency shifts induced by magnetic fields and strain or temperature; magnetic fields induce a differential splitting between the two resonances, while strain shifts them both in common mode (as discussed in the main text). For cw ODMR strain imaging, a camera acquires a wide-field image of the fluorescence intensity at each applied MW drive frequency. The combination of these images gives a MW spectrum for each pixel in the camera field of view; these spectra are fitted to Lorentzian line shapes to determine the frequencies of Eq. (F2) and to obtain maps of $(D + M_z)$ and B_z. The temperature-dependent zero-field splitting D and the axial-stress-induced frequency shift M_z are then separated as in the main text, by assuming the temperature to be constant across the field of view and the strain to be constant with time; subtracting the mean value across a field of view thus gives a map of the relative strain in the diamond. Figure 8(b) shows one such cw ODMR map, of diamond section B used in this work. Pixels with large strain gradients, such as the region shown in Fig. 4(d) of the main text, also affect cw ODMR, in this case via deviations from Lorentzian line shapes that interfere with the fitting procedure; Fig. 8(d) shows a map of fit residuals for the strain map of Fig. 8(c).

The measurement parameters used and the strain sensitivity achieved in this cw ODMR measurement both parallel those previously published in Ref. [16]. In those previous measurements, a strain-measurement precision of approximately 5×10^{-8} has been reached with a 3-h averaging time using a 13-μm-thick N-V–rich diamond overgrowth layer. The optimal lateral spatial resolution reported in those measurements was 1 μm, giving a minimal interrogation volume of 13 μm^3 per pixel and a corresponding volume-normalized strain sensitivity of $2 \times 10^{-5}/\sqrt{\text{Hz}\ \mu\text{m}^{-3}}$.

For further discussion of cw ODMR strain imaging, including simultaneous vector measurements of all four N-V classes, see Ref. [16].

[1] E. V. Levine, M. J. Turner, P. Kehayias, C. A. Hart, N. Langellier, R. Trubko, D. R. Glenn, R. R. Fu, and R. L. Walsworth, Principles and techniques of the quantum diamond microscope, Nanophotonics **8**, 1945 (2019).

[2] J. Maze, P. Stanwix, J. Hodges, S. Hong, J. Taylor, P. Cappellaro, L. Jiang, M. Dutt, E. Togan, A. Zibrov, A. Yacoby, R. Walsworth, and M. Lukin, Nanoscale magnetic sensing with an individual electronic spin in diamond, Nature **455**, 644 (2008).

[3] G. Balasubramanian, I. Y. Chan, R. Kolesov, M. Al-Hmoud, J. Tisler, C. Shin, C. Kim, A. Wojcik, P. R. Hemmer, A. Krueger, T. Hanke, A. Leitenstorfer, R. Bratschitsch, F. Jelezko, and J. Wrachtrup, Nanoscale imaging magnetometry with diamond spins under ambient conditions, Nature **455**, 648 (2008).

[4] J. M. Taylor, P. Cappellaro, L. Childress, L. Jiang, D. Budker, P. R. Hemmer, A. Yacoby, R. Walsworth, and M. D. Lukin, High-sensitivity diamond magnetometer with nanoscale resolution, Nat. Phys. **4**, 810 (2008).

[5] L. Rondin, J.-P. Tetienne, T. Hingant, J.-F. Roch, P. Maletinsky, and V. Jacques, Magnetometry with nitrogen-vacancy defects in diamond, Rep. Prog. Phys. **77**, 056503 (2014).

[6] R. Schirhagl, K. Chang, M. Loretz, and C. L. Degen, Nitrogen-vacancy centers in diamond: Nanoscale sensors for physics and biology, Annu. Rev. Phys. Chem. **65**, 83 (2014).

[7] J. F. Barry, J. M. Schloss, E. Bauch, M. J. Turner, C. A. Hart, L. M. Pham, and R. L. Walsworth, Sensitivity optimization for NV-diamond magnetometry, Rev. Mod. Phys. **92**, 015004 (2020).

[8] N. Arunkumar, D. B. Bucher, M. J. Turner, P. TomHon, D. Glenn, S. Lehmkuhl, M. D. Lukin, H. Park, M. S. Rosen, T. Theis, and R. L. Walsworth, Micron-scale NV-NMR spectroscopy with signal amplification by reversible exchange, PRX Quantum **2**, 010305 (2021).

[9] M. Pompili, S. L. N. Hermans, S. Baier, H. K. C. Beukers, P. C. Humphreys, R. N. Schouten, R. F. L. Vermeulen, M. J. Tiggelman, L. dos Santos Martins, B. Dirkse, S. Wehner, and R. Hanson, Realization of a multinode quantum network of remote solid-state qubits, Science **372**, 259 (2021).

[10] M. K. Bhaskar, R. Riedinger, B. Machielse, D. S. Levonian, C. T. Nguyen, E. N. Knall, H. Park, D. Englund, M. Lončar, D. D. Sukachev, and M. D. Lukin, Experimental demonstration of memory-enhanced quantum communication, Nature **580**, 60 (2020).

[11] G. Balasubramanian, P. Neumann, D. Twitchen, M. Markham, R. Kolesov, N. Mizuochi, J. Isoya, J. Achard, J. Beck, J. Tissler, V. Jacques, P. R. Hemmer, F. Jelezko, and J. Wrachtrup, Ultralong spin coherence time in isotopically engineered diamond, Nat. Mater. **8**, 383 (2009).

[12] M. W. Doherty, N. B. Manson, P. Delaney, F. Jelezko, J. Wrachtrup, and L. C. L. Hollenberg, The nitrogen-vacancy colour centre in diamond, Phys. Rep. **528**, 1 (2013).

[13] A. M. Edmonds, *et al.*, Characterisation of CVD diamond with high concentrations of nitrogen for magnetic-field sensing applications, Mater. Quantum Technol. **1**, 025001 (2021).

[14] A. Sipahigil, R. E. Evans, D. D. Sukachev, M. J. Burek, J. Borregaard, M. K. Bhaskar, C. T. Nguyen, J. L. Pacheco, H. A. Atikian, C. Meuwly, R. M. Camacho, F. Jelezko, E. Bielejec, H. Park, M. Lončar, and M. D. Lukin, An integrated diamond nanophotonics platform for quantum-optical networks, Science **354**, 847 (2016).

[15] C. T. Nguyen, D. D. Sukachev, M. K. Bhaskar, B. Machielse, D. S. Levonian, E. N. Knall, P. Stroganov, C. Chia, M. J. Burek, R. Riedinger, H. Park, M. Loncar, and M. D. Lukin, An integrated nanophotonic quantum register based on silicon-vacancy spins in diamond, Phys. Rev. B **100**, 165428 (2019).

[16] P. Kehayias, M. J. Turner, R. Trubko, J. M. Schloss, C. A. Hart, M. Wesson, D. R. Glenn, and R. L. Walsworth, Imaging crystal stress in diamond using ensembles of

nitrogen-vacancy centers, Phys. Rev. B **100**, 174103 (2019).

[17] S. B. van Dam, M. Walsh, M. J. Degen, E. Bersin, S. L. Mouradian, A. Galiullin, M. Ruf, M. IJspeert, T. H. Taminiau, R. Hanson, and D. R. Englund, Optical coherence of diamond nitrogen-vacancy centers formed by ion implantation and annealing, Phys. Rev. B **99**, 161203(R) (2019).

[18] S. Meesala, *et al.*, Strain engineering of the silicon-vacancy center in diamond, Phys. Rev. B **97**, 205444 (2018).

[19] S. Knauer, J. P. Hadden, and J. G. Rarity, *In-situ* measurements of fabrication induced strain in diamond photonic-structures using intrinsic colour centres, npj Quantum Inf. **6**, 1 (2020).

[20] D. Broadway, B. Johnson, M. Barson, S. Lillie, N. Dontschuk, D. McCloskey, A. Tsai, T. Teraji, D. Simpson, A. Stacey, J. McCallum, J. Bradby, M. Doherty, L. Hollenberg, and J.-P. Tetienne, Microscopic imaging of the stress tensor in diamond using *in situ* quantum sensors, Nano Lett. **19**, 4543 (2019).

[21] M. E. Trusheim and D. Englund, Wide-field strain imaging with preferentially aligned nitrogen-vacancy centers in polycrystalline diamond, New J. Phys. **18**, 123023 (2016).

[22] S. D. Bennett, N. Y. Yao, J. Otterbach, P. Zoller, P. Rabl, and M. D. Lukin, Phonon-Induced Spin-Spin Interactions in Diamond Nanostructures: Application to Spin Squeezing, Phys. Rev. Lett. **110**, 156402 (2013).

[23] Z. Xu, Z.-Q. Yin, Q. Han, T. Li, T. Li, T. Li, and T. Li, Quantum information processing with closely-spaced diamond color centers in strain and magnetic fields [invited], Opt. Mater. Express **9**, 4654 (2019).

[24] D. A. Golter, T. Oo, M. Amezcua, K. A. Stewart, and H. Wang, Optomechanical Quantum Control of a Nitrogen-Vacancy Center in Diamond, Phys. Rev. Lett. **116**, 143602 (2016).

[25] E. R. MacQuarrie, T. A. Gosavi, N. R. Jungwirth, S. A. Bhave, and G. D. Fuchs, Mechanical Spin Control of Nitrogen-Vacancy Centers in Diamond, Phys. Rev. Lett. **111**, 227602 (2013).

[26] H. Y. Chen, S. A. Bhave, and G. D. Fuchs, Acoustically Driving the Single-Quantum Spin Transition of Diamond Nitrogen-Vacancy Centers, Phys. Rev. Appl. **13**, 054068 (2020).

[27] M. S. J. Barson, P. Peddibhotla, P. Ovartchaiyapong, K. Ganesan, R. L. Taylor, M. Gebert, Z. Mielens, B. Koslowski, D. A. Simpson, L. P. McGuinness, J. McCallum, S. Prawer, S. Onoda, T. Ohshima, A. C. Bleszynski Jayich, F. Jelezko, N. B. Manson, and M. W. Doherty, Nanomechanical sensing using spins in diamond, Nano Lett. **17**, 1496 (2017).

[28] A. Barfuss, M. Kasperczyk, J. Kölbl, and P. Maletinsky, Spin-stress and spin-strain coupling in diamond-based hybrid spin oscillator systems, Phys. Rev. B **99**, 174102 (2019).

[29] K. O. Ho, M. Y. Leung, Y. Jiang, K. P. Ao, W. Zhang, K. Y. Yip, Y. Y. Pang, K. C. Wong, S. K. Goh, and S. Yang, Probing Local Pressure Environment in Anvil Cells with Nitrogen-Vacancy (N-V^{-}) Centers in Diamond, Phys. Rev. Appl. **13**, 024041 (2020).

[30] K. O. Ho, M. Y. Leung, Y. Y. Pang, K. C. Wong, P. H. Ng, and S. Yang, *In situ* studies of stress environment in amorphous solids using negatively charged nitrogen vacancy (NV^{-}) centers in nanodiamond, ACS Appl. Polym. Mater. **3**, 162 (2021).

[31] S. Rajendran, N. Zobrist, A. O. Sushkov, R. Walsworth, and M. Lukin, A method for directional detection of dark matter using spectroscopy of crystal defects, Phys. Rev. D **96**, 035009 (2017).

[32] M. C. Marshall, M. J. Turner, M. J.-H. Ku, D. F. Phillips, and R. L. Walsworth, Directional detection of dark matter with diamond, Quantum Sci. Technol. **6**, 024011 (2021).

[33] I. Friel, S. L. Clewes, H. K. Dhillon, N. Perkins, D. J. Twitchen, and G. A. Scarsbrook, Control of surface and bulk crystalline quality in single crystal diamond grown by chemical vapour deposition, Diamond Relat. Mater. **18**, 808 (2009). Proceedings of Diamond 2008, the 19th European Conference on Diamond, Diamond-Like Materials, Carbon Nanotubes, Nitrides and Silicon Carbide.

[34] M. Moore, Imaging diamond with X-rays, J. Phys.: Condens. Matter **21**, 364217 (2009).

[35] M. C. Marshall, D. F. Phillips, M. J. Turner, M. J. H. Ku, T. Zhou, N. Delegan, F. J. Heremans, M. V. Holt, and R. L. Walsworth, Scanning X-Ray Diffraction Microscopy for Diamond Quantum Sensing, Phys. Rev. Appl. **16**, 054032 (2021).

[36] A. Crisci, F. Baillet, M. Mermoux, G. Bogdan, M. Nesládek, and K. Haenen, Residual strain around grown-in defects in CVD diamond single crystals: A 2D and 3D Raman imaging study, Phys. Status Solidi A **208**, 2038 (2011).

[37] W. B. Alexander, P. H. Holloway, J. Simmons, and R. Ochoa, Increased precision in strain measurement of diamond by microRaman spectroscopy, J. Vac. Sci. Technol. A **12**, 2943 (1994).

[38] L. T. M. Hoa, T. Ouisse, D. Chaussende, M. Naamoun, A. Tallaire, and J. Achard, Birefringence microscopy of unit dislocations in diamond, Cryst. Growth Des. **14**, 5761 (2014).

[39] D. R. Glenn, R. R. Fu, P. Kehayias, D. L. Sage, E. A. Lima, B. P. Weiss, and R. L. Walsworth, Micrometer-scale magnetic imaging of geological samples using a quantum diamond microscope, Geochem. Geophys. Geosyst. **18**, 3254 (2017).

[40] D. R. Glenn, K. Lee, H. Park, R. Weissleder, A. Yacoby, M. D. Lukin, H. Lee, R. L. Walsworth, and C. B. Connolly, Single-cell magnetic imaging using a quantum diamond microscope, Nat. Methods **12**, 736 (2015).

[41] N. B. Manson, J. P. Harrison, and M. J. Sellars, Nitrogen-vacancy center in diamond: Model of the electronic structure and associated dynamics, Phys. Rev. B **74**, 104303 (2006).

[42] V. M. Acosta, E. Bauch, M. P. Ledbetter, A. Waxman, L.-S. Bouchard, and D. Budker, Temperature Dependence of the Nitrogen-Vacancy Magnetic Resonance in Diamond, Phys. Rev. Lett. **104**, 070801 (2010).

[43] G. Balasubramanian, A. Lazariev, S. R. Arumugam, and D.-W. Duan, Nitrogen-vacancy color center in diamond—emerging nanoscale applications in bioimaging and biosensing, Curr. Opin. Chem. Biol. **20**, 69 (2014).

[44] A. Boretti, L. Rosa, J. Blackledge, and S. Castelletto, Nitrogen-vacancy centers in diamond for nanoscale magnetic resonance imaging applications, Beilstein J. Nanotechnol. **10**, 2128 (2019).

[45] E. Moreva, E. Bernardi, P. Traina, A. Sosso, S. D. Tchernij, J. Forneris, F. Picollo, G. Brida, Z. Pastuović, I. P. Degiovanni, P. Olivero, and M. Genovese, Practical Applications of Quantum Sensing: A Simple Method to Enhance the Sensitivity of Nitrogen-Vacancy-Based Temperature Sensors, Phys. Rev. Appl. **13**, 054057 (2020).

[46] G. Kucsko, P. C. Maurer, N. Y. Yao, M. Kubo, H. J. Noh, P. K. Lo, H. Park, and M. D. Lukin, Nanometre-scale thermometry in a living cell, Nature **500**, 54 (2013).

[47] D. M. Toyli, C. F. D. L. Casas, D. J. Christle, V. V. Dobrovitski, and D. D. Awschalom, Fluorescence thermometry enhanced by the quantum coherence of single spins in diamond, Proc. Natl. Acad. Sci. **110**, 8417 (2013).

[48] P. Neumann, I. Jakobi, F. Dolde, C. Burk, R. Reuter, G. Waldherr, J. Honert, T. Wolf, A. Brunner, J. Shim, D. Suter, H. Sumiya, J. Isoya, and J. Wrachtrup, High-precision nanoscale temperature sensing using single defects in diamond, Nano Lett. **13**, 2738 (2013).

[49] C. L. Degen, F. Reinhard, and P. Cappellaro, Quantum sensing, Rev. Mod. Phys. **89**, 035002 (2017).

[50] E. Bauch, S. Singh, J. Lee, C. A. Hart, J. M. Schloss, M. J. Turner, J. F. Barry, L. M. Pham, N. Bar-Gill, S. F. Yelin, and R. L. Walsworth, Decoherence of ensembles of nitrogen-vacancy centers in diamond, Phys. Rev. B **102**, 134210 (2020).

[51] J. Wang, F. Feng, J. Zhang, J. Chen, Z. Zheng, L. Guo, W. Zhang, X. Song, G. Guo, L. Fan, C. Zou, L. Lou, W. Zhu, and G. Wang, High-sensitivity temperature sensing using an implanted single nitrogen-vacancy center array in diamond, Phys. Rev. B **91**, 155404 (2015).

[52] When used for single–N-V thermometry in Ref. [47,51], this pulse sequence was referred to as the T-CPMG or thermal Carr-Purcell-Meiboom-Gill sequence.

[53] P. Konzelmann, T. Rendler, V. Bergholm, A. Zappe, V. Pfannenstill, M. Garsi, F. Ziem, M. Niethammer, M. Widmann, S.-Y. Lee, P. Neumann, and J. Wrachtrup, Robust and efficient quantum optimal control of spin probes in a complex (biological) environment: Towards sensing of fast temperature fluctuations, New J. Phys. **20**, 123013 (2018).

[54] P. Udvarhelyi, V. O. Shkolnikov, A. Gali, G. Burkard, and A. Pályi, Spin-strain interaction in nitrogen-vacancy centers in diamond, Phys. Rev. B **98**, 075201 (2018).

[55] D. J. Twitchen, C. S. J. Pickles, S. E. Coe, R. S. Sussmann, and C. E. Hall, Thermal conductivity measurements on CVD diamond, Diamond Relat. Mater. **10**, 731 (2001). 11th European Conference on Diamond, Diamond-like Materials, Carbon Nanotubes, Nitrides and Silicon Carbide.

[56] D. Allan, Statistics of atomic frequency standards, Proc. IEEE **54**, 221 (1966).

[57] M. J. H. Ku, T. X. Zhou, Q. Li, Y. J. Shin, J. K. Shi, C. Burch, L. E. Anderson, A. T. Pierce, Y. Xie, A. Hamo, U. Vool, H. Zhang, F. Casola, T. Taniguchi, K. Watanabe, M. M. Fogler, P. Kim, A. Yacoby, and R. L. Walsworth, Imaging viscous flow of the Dirac fluid in graphene, Nature **583**, 537 (2020).

[58] C. A. Hart, J. M. Schloss, M. J. Turner, P. J. Scheidegger, E. Bauch, and R. L. Walsworth, N-V—Diamond Magnetic Microscopy Using a Double Quantum 4-Ramsey Protocol, Phys. Rev. Appl. **15**, 044020 (2021).

[59] H. J. Mamin, M. Kim, M. H. Sherwood, C. T. Rettner, K. Ohno, D. D. Awschalom, and D. Rugar, Nanoscale nuclear magnetic resonance with a nitrogen-vacancy spin sensor, Science **339**, 557 (2013).

[60] D. Le Sage, K. Arai, D. R. Glenn, S. J. DeVience, L. M. Pham, L. Rahn-Lee, M. D. Lukin, A. Yacoby, A. Komeili, and R. L. Walsworth, Optical magnetic imaging of living cells, Nature **496**, 486 (2013).